Urban Subsidence Monitoring Using Radar Interferometry: Algorithms and Validation

Michele Crosetto, Manuel Castillo, and Roman Arbiol

Abstract

The differential interferometric SAR (DInSAR) technique has proved its capability to detect small surface deformations in several types of applications. In this paper, its use as a quantitative subsidence monitoring tool is addressed to. A complete procedure is described, giving emphasis to the algorithms that have a major impact on the quality of the DInSAR results: the calibration of the InSAR geometry based on ground control points, which guarantees a high accuracy of the InSAR geometric model; a filtering procedure suitable to reduce the atmospheric effects in small-scale subsidences; and a data fusion procedure for multiple observations, which represents a key step to improve the quality of the DInSAR products. The procedure was used in the analysis of a small-scale urban subsidence located in Catalonia, northeastern Spain. The validation of the results, which was based on the comparison with precise and independent reference data, is discussed in detail.

Introduction

The interferometric SAR (synthetic aperture radar), InSAR, is a remote sensing technique used for applications such as the generation of digital elevation models (DEMs), the monitoring of surface movements and deformations, and thematic mapping. InSAR DEM generation is particularly valuable for the topographic mapping of regions characterized by persistent cloud cover, due to the all-weather capability of the radar. The best results are achieved with the so-called one-pass InSAR, which is insensitive to surface decorrelation and to atmospheric effects.

The InSAR phase is sensitive to terrain topography and to relative changes in elevation occurring between two SAR antenna passes over the same area. If the terrain topography is known, i.e., a DEM is available, the corresponding phase component can be subtracted from the InSAR phase, leaving the component due to the terrain surface deformation: this makes the detection of subtle deformations of the Earth's crust possible. The DInSAR technique, based on spaceborne SAR data, has been successfully employed in different application fields; see, for a review, Hanssen (2001): glacier dynamics (Goldstein *et al.*, 1993; Kwok and Fahnestock, 1996); earthquakes (Massonnet *et al.*, 1993; Massonnet *et al.*, 1994); volcanoes (Massonnet *et al.*, 1995; Amelung *et al.*, 2000); landslides (Carnec *et al.*, 1996; Kimura and Yamaguchi, 2000); and the anthropogenic deformations related to water resource exploitation, mining activity, and construction works (Amelung *et al.*, 1999; Tesauro *et al.*, 2000).

The use of spaceborne DInSAR is however affected by some important limitations, such as temporal decorrelation and the effects caused by different atmospheric conditions (atmospheric effects). In the following, the limitations related to the temporal evolution, planimetric extension, and the magnitude of the considered deformations are briefly outlined. The phenomena that are characterized by very slow deformation rates (e.g., a few millimeters per year) are detectable only over large time intervals, where the SAR images usually have very low correlation (low coherence). An exception occurs in urban areas, where a high image correlation may be observed even over large periods. SAR resolution represents a second limitation. Using a typical six-look azimuth compression, ERS-1 and -2 images are characterized by a pixel footprint of about 20 by 24 m. In order to avoid aliasing, an adequate sampling of a given deformation field has to be guaranteed: this poses a limit on the minimum size of the deformations that are detectable by DInSAR. The interferometric phase noise, due to different sources of image decorrelation, represents a further limitation of DInSAR. Under the best conditions, the standard deviation of the C-band ERS DInSAR observations is on the order of a few millimeters, while it can be severely degraded in low coherence areas. This aspect is critical for all applications characterized by small deformation magnitudes.

The Institut Cartogràfic de Catalunya (ICC) has implemented its own DInSAR processing chain, whose most original components are described in this paper. Emphasis is given to the InSAR geometric aspects, which play a key role for the quantitative DInSAR applications; to a filtering procedure suitable for reducing the atmospheric effects in small-scale subsidences; and to a data fusion procedure for multiple observations of the same phenomenon. The processing chain was validated on a suitable test area, located in Catalonia, northeastern Spain. The case study includes all the above-mentioned critical characteristics: a slow deformation rate, a small spatial extent, and a moderate total deformation magnitude. Furthermore, it concerns an urban subsidence monitoring: a DInSAR application related to risk assessment and public safety, which requires high quality standards. In different papers, DInSAR accuracies of few a millimeters are claimed; see, e.g., Strozzi *et al.*, (2001) and Peltzer and Rosen (1995). However, due to a relative lack of independent data, the validation of the DInSAR products is often not provided. In this paper, emphasis is given to the quantitative validation of the DInSAR results, based on the comparison with precise and independent geodetic data.

The paper begins with a concise description of the ICC DInSAR procedure. This is followed by a discussion of the

Unitat de Teledetecció, Institut Cartogràfic de Catalunya, Parc de Montjuïc, 08038 Barcelona, Spain.

M. Crosetto is currently with the Institute of Geomatics, Campus de Castelldefels, 08860 Castelldefels (Barcelona), Spain (michele.crosetto@ideg.es).

Photogrammetric Engineering & Remote Sensing
Vol. 69, No. 7, July 2003, pp. 775–783.

0099-1112/03/6907–775$3.00/0

InSAR geometric aspects. The fourth section describes the procedure for the reduction of atmospheric effects, while the data fusion procedure is illustrated in the fifth section. The sixth section describes the test case, providing the analysis and interpretation of the validation results. Conclusions follow.

DInSAR Procedure

The ICC DInSAR procedure, at present only used with ERS-1 and -2 images, shares most of its components with the DEM generation procedure. It includes seven main processing stages, as it is concisely detailed below.

- **Image Registration.** Image registration is based on homologous points, extracted through the maximization of the complex image coherence. A large set of points, say a few hundreds for a 100- by 100-km scene, guarantees a robust image registration with sub-pixel accuracy. Problems with the current procedure could occur with long-time interferograms and low-coherence scenes. In these cases, image registration techniques based on the cross-correlation of the image amplitudes could be more effective. For a review of different image registration algorithms, see Hanssen (2001).
- **InSAR Geometry Calibration.** The InSAR geometric model, which connects the image space to the object space, is employed in the interferogram simulation and the geocoding of the InSAR products. An accurate geometric model is derived using a least-squares (LS) calibration procedure based on ground control points (GCPs).
- **Interferogram Simulation.** The topographic interferogram simulation is based on a DEM of the imaged scene and the InSAR geometric model. The DInSAR phase, which contains the information related to terrain surface deformation, is obtained by subtracting the simulated interferogram from the real interferogram.
- **Phase Unwrapping.** Three different phase unwrapping methods are implemented: region growing, least squares, and weighted least squares (Ghiglia and Pritt, 1998). In order to reduce the phase noise due to image decorrelation and improve the phase unwrapping performance, different filtering procedures can be employed. With the images described in the test case, the best results were achieved with the adaptative filter proposed by Goldstein and Werner (1998).
- **Atmospheric Effect Assessment and Reduction.** Atmospheric effects may severely degrade the information content of the DInSAR phase. In order to reduce these effects, an original procedure is employed, which is suitable for DInSAR applications of small spatial extent.
- **Deformation Map Generation.** In this step, which includes the phase-to-deformation transformation and the geocoding, the geocoded subsidence map and its associated quality map are generated. Some DInSAR applications, e.g., those related to glacier dynamics, involve 3D deformations. In this work, the horizontal components of the deformations are not considered. The quality map provides, for each pixel, the standard deviation of the measured deformation, which is estimated as a function of the image coherence (Bamler and Hartl, 1998).
- **Fusion of Multiple Deformation Maps.** Multiple DInSAR observations of the same subsidence may sometimes be available. In order to improve the quality of the DInSAR output, a suitable data fusion procedure is used, which receives as input the multiple deformation maps and the corresponding quality maps.

The following three sections describe in detail the most original components of the ICC DInSAR procedure: the InSAR geometric aspects, the assessment and reduction of the atmospheric effects, and the data fusion procedure.

InSAR Geometric Aspects

As in most remote sensing techniques, DInSAR requires an accurate geometric model to connect the image space to the object space: in the image space are given the original SAR images and the interferograms, while in the object space are defined the DInSAR output products, such as geocoded subsidence maps. The geometric model is required in two key processing stages: the interferogram simulation, which involves the object-to-image transformation, and the deformation map generation, which is based on the image-to-object transformation. This section focuses on two aspects related to the InSAR geometry: the calibration of the geometric model and the interferogram simulation.

The InSAR geometry is depicted in Figure 1. The master satellite M, the slave satellite S, and a generic pixel footprint P are usually defined in a geocentric Cartesian system. The image coordinates of a given pixel—azimuth and range (az, rg)—are connected to the object space coordinates (x,y,z) through the time equation (Equation 1), the range equation (Equation 2), and the Doppler equation (Equation 3), as shown in Figure 1. Equation 1 provides the acquisition time T of the considered pixel, used to compute the corresponding satellite position. Equations 2 and 3 refer to the master M; however, all three equations hold for S. These equations include important parameters such as the first line acquisition time T_0, the azimuth pixel size ΔT, the near slant range SR_0, the range pixel size ΔSR, the master velocity vector $\vec{V}_M$, the radar wavelength λ, and the Doppler frequency of the master image $f_{D\,M}$. These parameters, which are included in the auxiliary data of the SAR images, are usually known with an inadequate accuracy. Their direct use in the model may result in important distortions in the transformations between the image and object spaces. In order to get an accurate geometric model, the model parameters have to be refined by an LS adjustment using GCPs. Adopting a model similar to that described in Tannous and Pikeroen (1994), the following parameters are refined in the calibration: R_0, T_0, ΔT, and $f_{D\,M}$. The first three are assumed to be constant for a given scene, while for $f_{D\,M}$ a linear variation over a SAR image is considered. Therefore, six parameters for each image are refined. It must be noted that the orbit parameters are not included in the calibration. A detailed discussion of the model can be found in the final report of the project ORFEAS (Patias, 1998). If available, the precise orbits have to be used. However, the above six parameters are sufficient to compensate for the orbit errors, even if preliminary orbits are employed. The described calibration does not make use of the interferometric phase. This represents an original feature with respect to the approaches used in different commercial software packages (e.g., Atlantis, ERDAS, Sarmap, etc.) or described in the literature (e.g., Hellwich and Ebner (2000) and Crosetto (2002a)). The advantage of the proposed procedure is that the phase noise, atmospheric effects, and the unwrapping-related errors have no influence on the calibration, thus avoiding the risk of a biased parameter estimation.

The original implementation of the calibration worked with one image at the time, i.e., on each image of an InSAR pair, separately. The procedure is now extended in order to fuse data coming from multiple images (multiple LS adjustment), e.g., ascending and descending pairs of SAR images. The multiple LS adjustment allows reducing the number of required GCPs by using tie points, analogous to procedures used in photogrammetry. The InSAR calibration represents a fundamental step in the ICC procedure, which guarantees a high accuracy of the model. In order to assure a sufficient redundancy, at least 10 to 15 GCPs for a 100- by 100-km scene have to be collected. This operation may be time-consuming, due to the difficulties related to the point identification in the SAR images.

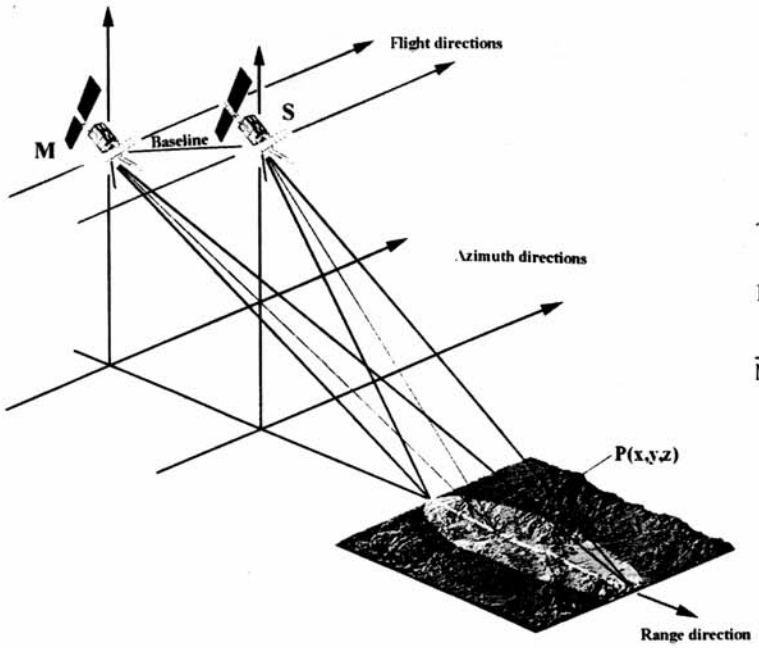

$$T = T_0 + \Delta T \cdot az \quad (1)$$

$$MP = SR_0 + \Delta SR \cdot rg \quad (2)$$

$$\overline{MP} \cdot \overline{V}_M = -\lambda \cdot MP \cdot \frac{f_{D\_M}}{2} \quad (3)$$

Figure 1. The InSAR geometry and the InSAR model: three equations that connect the image space to the object space.

After the LS calibration, the residuals on the GCPs are typically on the order of one pixel: using a six-look compression, this corresponds to about 24 m on the ground. In the test case, which is described in the last part of the paper, 27 GCPs were used for the calibration. Their distribution is sketched in Figure 2; because some of the GCPs are very close to each other, only 21 GCPs appear in the image. In the same figure, an enlargement of two GCPs, measured on a SAR amplitude image and on an orthoimage, is depicted. The quality of the InSAR geometric model directly affects the interferogram simulation, which is based on the transformation from the DEM (object space) to the simulated interferogram (image space). For this reason, the simulation is always performed after the InSAR calibration.

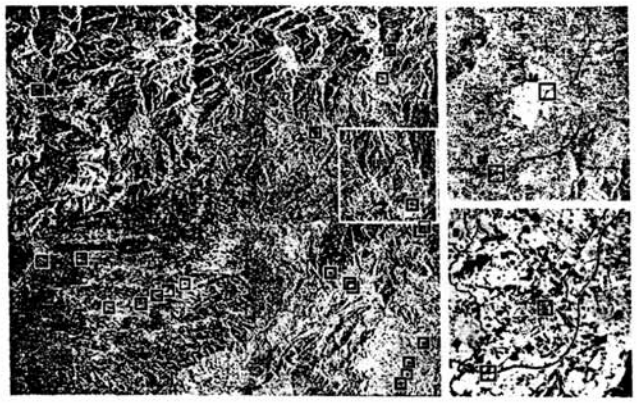

Figure 2. Distribution of the GCPs used in the test case. The whole scene covers 100 by 100 km. The white frame indicates the 20- by 25-km test case sub-scene. On the right, two GCPs located on a SAR amplitude image (above) and on an orthoimage (below) are shown.

The *a priori* known DEM represents a second important factor for the quality of the simulated interferogram, and hence for the quality of the derived subsidence map. A DEM error e_H results in a residual topographic component Φ_{RH} of the DInSAR phase, whose magnitude is modulated by the perpendicular baseline $B_\perp$ (the component of the distance MS measured perpendicular to the look direction). In Table 1, considering the ERS-1 and -2 parameters, the values of Φ_{RH} for different values of $B_\perp$ and e_H are reported. For small baselines the values of Φ_{RH} remain well below the typical phase noise level, which for the ERS InSAR pairs is on the order of 40 degrees (Hanssen, 2001): they are, therefore, practically undetectable. On the other hand, the use of a large baseline, e.g., greater than 250 m, imposes severe requirements on the quality of the employed DEMs. Note that large baselines are also critical for the geometric decorrelation.

Atmospheric Effect Assessment and Reduction

Atmospheric effects represent one of the major limits of SAR interferometry as a subsidence monitoring tool. To mitigate the degradation caused by these effects, multiple observations are sometimes used (Ferretti *et al.*, 2001). The ICC DInSAR chain includes an original procedure to reduce the atmospheric effects, which may be employed with a single image pair. The procedure takes advantage of the correlation characteristics of the atmospheric effects, and is suitable for DInSAR applications of small spatial extent. It is described in detail in Crosetto *et al.* (2002), where the results obtained on urban subsidences that are less than one kilometer wide are described. The main steps of the procedure are briefly outlined below.

- **Identification of Stable Areas.** Using *a priori* available information, stable areas in the vicinity of the deformation area under analysis have to be identified.
- **Atmospheric Effect Assessment.** The stable areas are used to perform a quantitative analysis of the atmospheric effects on a given interferogram. Over a generic subsidence area, the DInSAR phase Φ consists of the following components: the

TABLE 1. RESIDUAL TOPOGRAPHIC COMPONENT, IN DEGREES, FOR DIFFERENT VALUES OF $B_\perp$ AND e_H, COMPUTED USING THE ERS-1 AND -2 PARAMETERS

	$B_\perp$ = 0 m	$B_\perp$ = 10 m	$B_\perp$ = 50 m	$B_\perp$ = 100 m	$B_\perp$ = 250 m	$B_\perp$ = 400 m
e_H = 0.5 m	0.0°	0.2°	1.1°	2.2°	5.4°	8.6°
e_H = 1.0 m	0.0°	0.4°	2.2°	4.3°	10.8°	17.2°
e_H = 2.0 m	0.0°	0.9°	4.3°	8.6°	21.5°	34.4°
e_H = 5.0 m	0.0°	2.2°	10.8°	21.5°	53.8°	86.0°
e_H = 10.0 m	0.0°	4.3°	21.5°	43.0°	107.5°	172.1°
e_H = 20.0 m	0.0°	8.6°	43.0°	86.0°	215.1°	344.1°

deformation component Φ_D, the atmospheric contribution Φ_A, the residual topographic component Φ_{RH}, and the decorrelation noise Φ_N (Ferretti *et al.*, 2001). Considering the stable areas, where Φ_D is naught, it is possible to evaluate the influence of Φ_A on the interferogram at hand. In case the atmospheric delay is constant over the interferogram (i.e., there are no atmospheric effects), Φ consists of Φ_{RH} and Φ_N, which can be considered spatially decorrelated (they are referred to as the noise). As far as Φ_{RH} is concerned, this assumption holds for high quality DEMs, e.g., the high resolution DEMs derived by aerial photogrammetry, while it does not hold for INSAR DEMs, which are potentially affected by atmospheric effects. In the presence of atmospheric heterogeneities, Φ_A (which is referred to as the signal) represents the correlated part of Φ. Its contribution can be therefore assessed by analyzing the spatial autocorrelation of Φ. The analysis is performed using the autocovariance function of Φ, whose characteristic parameters are the variance of the signal σ_S^2 and the correlation length L_C. An interferogram weakly affected by atmospheric effects will be characterized by a nearly zero value of σ_S^2 and L_C, while in the presence of atmospheric heterogeneities the two parameters will be significantly different from zero. The above criterion can be used to classify, from the viewpoint of atmospheric effects, reliable and potentially degraded interferograms.

In Figure 3, the autocovariance functions of the four interferograms used in the test case are depicted. The values of the autocovariance functions, which were normalized by dividing by the total phase variance σ_Φ^2, indicate the spatial correlation of the DINSAR phase. The functions were computed over a stable area of about 500 by 600 m located in the vicinity of the subsidence area. Pair 4, which is the less affected by atmospheric effects, shows a very low spatial correlation and a small L_C.

- **Atmospheric Component Extraction over the Stable Areas.** Taking advantage of the above correlation characteristics, starting from the phase Φ, the atmospheric component Φ_A is extracted over the stable areas. This is achieved using the method of least-squares collocation, a flexible stochastic filtering technique widely employed in geodesy. Assuming the DINSAR phase over the stable areas to be a realization of a 2D stationary stochastic process, the collocation method separates the signal Φ_A from the noise (filtering), using the autocovariance function of the process, which is estimated from the original data. For a complete description of the LS collocation technique, see Moritz (1978) and Dermanis (1984). An example of the application of the collocation method to the study of vertical crustal movements can be found in El-Fiky *et al.* (1997). This stage is performed with the GRAVSOFT package of the University of Copenhagen (Tscherning *et al.*, 1994).
- **Atmospheric Component Prediction over the Subsidence Area.** Using the Φ values over the stable areas and the above-described autocovariance function, the collocation method can be used to predict the atmospheric component over the subsidence area (signal prediction). This represents the most critical step of the procedure, which suffers for its intrinsic limitation related to the non-stationarity of the analyzed signal that practically confines its use to the vicinity of the stable areas.
- **Phase Correction.** In the subsidence area, the predicted signal Φ_{A_P} is subtracted from the original phase Φ, hence reducing the atmospheric effects. After the correction, only a residual component, $\Phi_A - \Phi_{A_P}$, will affect the interferometric phase. Its magnitude basically depends on the prediction distance, i.e., the distance between the stable and the subsidence areas.

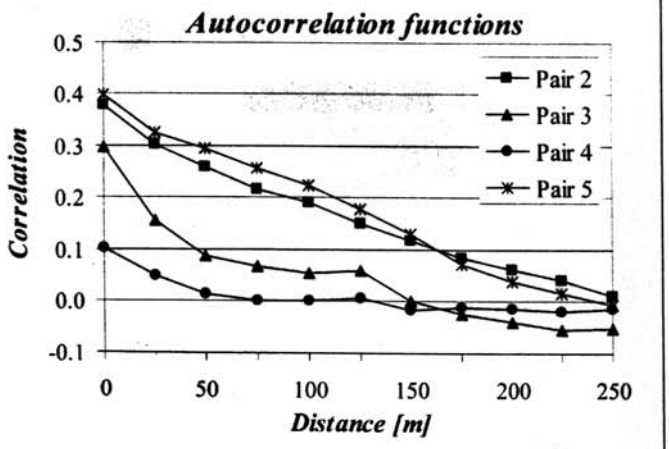

Figure 3. Autocovariance functions of the four interferograms used in the test case, computed over a stable area of 500 by 600 m, located in the vicinity of the subsidence area.

Data Fusion Procedure for Multiple DInSAR Observations

After the atmospheric effect reduction, the deformation map generated by DINSAR can be affected by different types of errors, like the decorrelation noise, the residual topographic component, the unwrapping-related errors, and the residual atmospheric component. These errors may severely degrade the monitoring capability of the DINSAR technique. The use of multiple DINSAR observations of the same subsidence phenomenon offers a way to improve the precision and the reliability of the derived DINSAR products. The data fusion can be performed either on co-registered interferograms (image space) or on subsidence maps (object space). The ICC chain includes a data fusion procedure which works with multiple subsidence maps.

The surface deformation of a generic subsidence may be described by a variable $D = f(X,Y,t)$, defined in a 3D domain, where X and Y are two planimetric components and t is the time. In order to fuse multiple observations, a 3D model, which is suitable to describe the subsidence, has to be chosen. In the following, a simple model is adopted, which describes the subsidence variation in planimetry by bilinear splines, and has a linear temporal evolution. This model was considered adequate for the analysis of the test case, where, using external information, the subsidence rate may be assumed to be constant. In a more general case, an extension of the model could be required. A scheme of the data fusion procedure is shown in Figure 4. The input data are a set of deformation maps and the corresponding quality maps. The input maps have to be accurately geolocated with respect to the same reference system. This is obtained by performing the INSAR calibration in the genera-

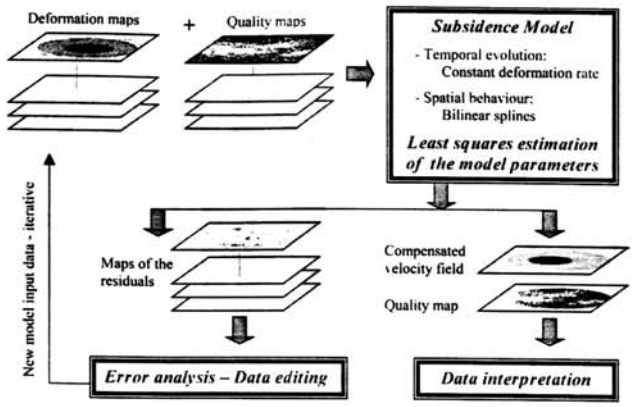

Figure 4. Scheme of the data fusion procedure for multiple DInSAR observations based on a simple subsidence model.

tion of each individual map. The accurate geolocation makes the fusion of subsidence maps coming from ascending and descending SAR images possible. The data fusion procedure takes into account the weight associated with each individual DInSAR observation, which is derived from the quality maps. The data fusion outputs, which are estimated by LS adjustment, include the compensated velocity field, the corresponding quality map, and the maps of the residuals (difference between observed and compensated values). An automatic outlier rejection procedure, the data snooping of Baarda (1968), is implemented. The residuals may be used to improve the unwrapped phases or check the residual atmospheric effects (data editing), obtaining new input data. In order to derive better data fusion outputs, the data fusion procedure can be run iteratively.

Description of the Sallent Test Case

The DInSAR procedure was validated over an urban subsidence of small spatial extent, located in the village of Sallent, about 60 km north of Barcelona in northeastern Spain (see Figure 5). A portion of the village, which lies on an old pottassic salt mine, is subjected to subsidence, which is mainly caused by water filtration in the salt layers. Since July 1997 the subsidence is monitored monthly with a precise leveling network.

In order to monitor the subsidence using SAR interferometry, seven complex ERS images were acquired, which cover the time period from June 1995 to July 1999 (see Table 2). From the seven images, it is in principle possible to compute 21 different interferograms, where only six of them are linearly independent. However, only five interferograms have a normal baseline $B_\perp$ smaller then 300 to 400 m, a limit usually adopted for the interferometric pairs. Furthermore, one of these interferograms, built with the images 2 and 3 ($B_\perp$ = 101 m), had to be discharged due to its one-day separation, a short time period which is not af-

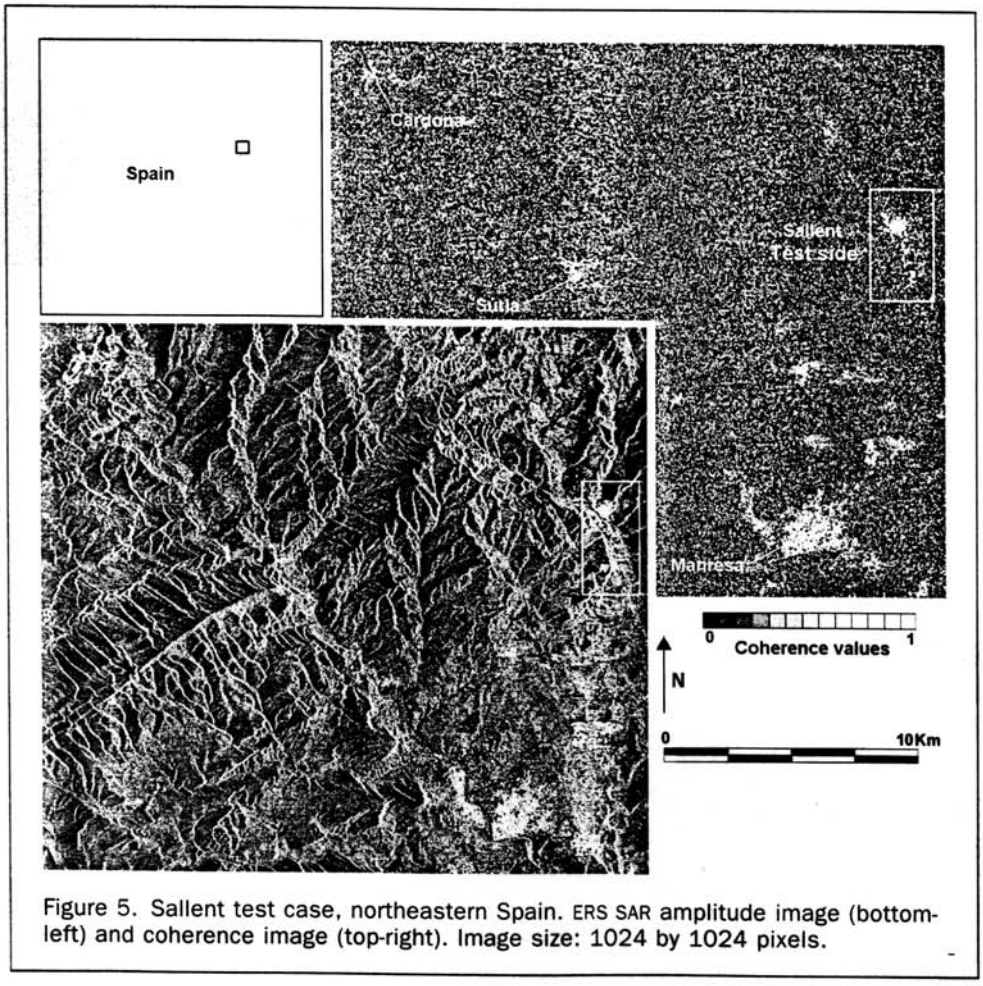

Figure 5. Sallent test case, northeastern Spain. ERS SAR amplitude image (bottom-left) and coherence image (top-right). Image size: 1024 by 1024 pixels.

TABLE 2. CHARACTERISTICS OF THE SEVEN COMPLEX SAR IMAGES USED IN THE TEST CASE (FIRST THREE COLUMNS) AND NORMAL BASELINES $B_\perp$ OF ALL POSSIBLE INTERFEROGRAMS, IN METERS

	Sensor	Acquisition Time	Im1	Im2	Im3	Im4	Im5	Im6	Im7
Image 1	ERS-1	13-Jun-1995 10:40:58 AM	—	978	877	439	**6**	446	884
Image 2	ERS-1	31-Oct-1995 10:40:59 AM		—	**101**	539	985	532	**107**
Image 3	ERS-2	01-Nov-1995 10:41:01 AM			—	438	884	431	**6**
Image 4	ERS-2	29-Jan-1997 10:40:52 AM				—	446	**8**	**432**
Image 5	ERS-2	18-Feb-1998 10:40:49 AM					—	453	878
Image 6	ERS-2	29-Apr-1998 10:40:51 AM						—	425
Image 7	ERS-2	27-Jul-1999 10:40:39 AM							—

TABLE 3. CHARACTERISTICS OF THE FOUR ERS INTERFEROMETRIC PAIRS USED IN THE SALLENT TEST CASE

Interferogram	Image Pair	ΔT [days]	$B_\perp$ [m]	Mean Coherence over the Sallent Urban Area
Pair 2	Images 3–7	1364	6	0.448
Pair 3	Images 1–5	981	6	0.399
Pair 4	Images 4–6	455	8	0.490
Pair 5	Images 2–7	1365	107	0.414

fected by any detectable surface movement. Therefore, only four pairs were processed (see Table 3).

Some of the processing steps, such as image registration and InSAR calibration, were performed on the original SAR images, while the other steps were performed on six-look azimuth compressed sub-images of 1024 by 1024 pixels, covering an area of about 20 by 25 km. The amplitude and coherence sub-images of Pair 3 are shown in Figure 5. In this figure, the white frames indicate the location of the Sallent test case. One may notice that a large portion of the coherence sub-image is characterized by low coherence values (the mean coherence is estimated to be 0.255). This is due to the large time interval of the interferogram, which in this case equals 981 days. The high coherence areas, which appear in lighter grey values, correspond to the urban areas.

The characteristics of the four processed interferometric pairs are reported in Table 3. One may observe that the mean coherence over the urban area of Sallent decreases with time: Pair 4, which is characterized by the shortest time interval, has the highest mean value. However, the mean coherence of Pair 3 is lower than that of Pair 2 and Pair 5. The temporal coverage of the four interferograms, compared with the available reference geodetic data, is sketched in Figure 6. The interferograms were separately processed. The InSAR calibration was performed using 27

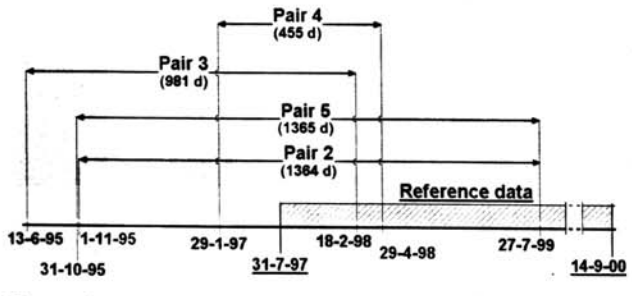

Figure 6. Temporal coverage of the four interferometric pairs and the geodetic reference data used in the validation.

GCPs (Figure 2), identified by an operator in one image and then automatically transferred to the other images by coherence maximization. The calibration proved to be effective even without the use of the ERS SAR precise orbits: all the results described in this work were obtained employing the preliminary orbits available in the auxiliary data of the SAR images. The interferogram simulation was performed employing a 15-m digital terrain model (DTM), generated at ICC as by-product of 1:5000-scale topographic map production and characterized by an RMS error of about 1 m. It must be noted that the simulation should be based on a DEM of the imaged scene, which describes the actual surface elevation (including vegetation, buildings, etc.), while a DTM only describes the terrain surface. However, considering the small baselines of the analyzed pairs (see Tables 1 and 3), the DTM was considered sufficient for the simulation purposes. The phase unwrapping of the four interferograms was performed taking the reference phase on the old town center of Sallent, a stable area that is located about 800 m from the subsidence center.

Validation of the Single Subsidence Maps

Over the village of Sallent, the four differential interferograms qualitatively show a coherent pattern: the DInSAR phase reaches its maximum magnitude near the Sallent railways station, an area whose subsidence is documented by geodetic surveys. It must be mentioned that this also occurs in correspondence to other villages of the same scene, such as Cardona and Súria (see Figure 5) that are known to be subject to subsidence. This first result confirms the DInSAR capability to discriminate, in urban areas and from the qualitative viewpoint, between subsidence and stable areas.

The DInSAR validation was performed separately on each subsidence map. The patterns of the four deformation fields are quite similar: they include an ellipse-shaped area of deformation, with length of axes on the order of 200 m and 300 m, respectively. The planimetric locations of the four maxima fit quite well with the reference one: the discrepancies are on the order of 2 to 3 pixels, i.e., 50 to 75 m. This confirms the good quality of the adopted InSAR models. The same cannot be said considering the magnitude of the maximum deformations. In Table 4, the deformations measured with the four pairs (third column) and the corresponding reference values (seventh column) are reported. The results for Pairs 3 and 4 are quite consistent with the reference values, while Pairs 2 and 5 show important discrepancies. It must be noted that these measures refer to time intervals that only partially overlap: from 1995 to 1999 for the DInSAR data and from July 1997 to September 2000 for the geodetic measures (Figure 6). The latter ones display a linear behavior of the subsidence: in order to perform the validation, they were linearly extrapolated to the corresponding time intervals of the four pairs. This operation could have introduced a bias, whose magnitude, however, should not be sufficient to explain the above discrepancies.

The atmospheric effects were considered as a possible

TABLE 4. MAGNITUDE OF THE MAXIMUM DEFORMATIONS OF THE SALLENT SUBSIDENCE: DInSAR VALUES BEFORE THE CORRECTION, ATMOSPHERIC CORRECTIONS, CORRECTED DInSAR VALUES WITH THEIR STANDARD DEVIATIONS, AND THE CORRESPONDING REFERENCE VALUES

	ΔT [days]	DInSAR Deformation before Correction [cm]	Correction [cm]	Corrected DInSAR [cm] Deformation	St. dev.	Reference [cm]
Pair 4	455	2.6	—	2.6	0.31	2.7
Pair 3	981	5.4	—	5.4	0.33	5.7
Pair 2	1364	4.2	2.6	6.8	0.89	7.9
Pair 5	1365	5.0	1.8	6.8	0.61	7.9

explanation of this behavior. The analysis of the interferometric pairs over a stable area, located about 300 m from the subsidence area, indicated the presence of atmospheric heterogeneities in Pairs 2 and 5 (see Figure 3): their spatial correlations have much higher values than those of the other two pairs. The correction of the atmospheric effects was performed on each of the four interferometric pairs, using the above stable area for the collocation filtering and prediction. It must be noted that the correction procedure on a pair which is not affected by atmospheric effects gives zero values for the predicted Φ_A and hence has no consequence. This was the case for Pairs 3 and 4, whose corrections gave nought values, while for Pairs 2 and 5 the corrections were significantly different from zero (see Table 4). A phase profile over Pair 2 is shown in Figure 7. The original phase Φ is affected by a strong atmospheric component, which in the left part of the stable area results in a bias up to about 2π. Over the stable area the corrected phase consists of a zero-mean noise, indicating that Φ_A was properly removed. The Φ_A was estimated by collocation filtering over the stable area (left side), and by collocation prediction over the subsidence area (right side). Over the maximum subsidence, the estimated correction equals 2.6 cm (5.4 rad). The results obtained after compensation of the atmospheric effects are reported in the fifth column of Table 4. For Pairs 2 and 5 there is a remarkable improvement with respect to the original results. It must be noted that the coincidence of the two corrected values—they both equal 6.8 cm (14.2 rad)—has to be considered fortuitous. It is interesting to consider the standard deviations associated with the corrected DInSAR measures (see Table 4, sixth column). These values, which are contained in the quality maps, consist of two terms: the standard deviation of the original DInSAR measure, estimated as a function of the coherence (for a review of different estimation methods, see Hanssen (2001)), and the standard deviation of the atmospheric correction, estimated through the LS collocation. Due to the comparable values of the four coherence images over the maximum deformation location, the first term is quite similar for the four pairs (about 0.3 cm). On the contrary, there are important differences concerning the second term: for Pairs 3 and 4 the standard deviation is nought (there was no correction), while it equals 0.84 cm and 0.53 cm for Pair 2 and Pair 5, respectively. These differences were automatically taken into account in the data fusion described in the following section.

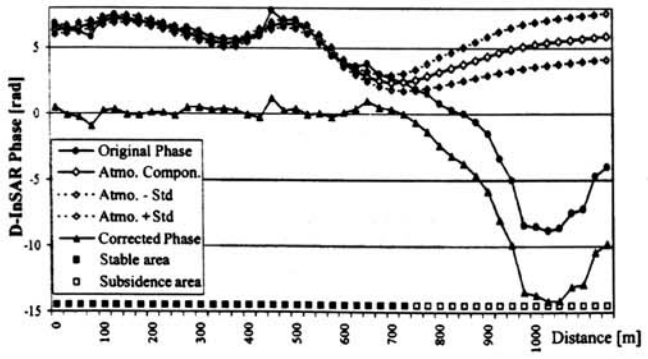

Figure 7. Reduction of the atmospheric effects over the subsidence of Sallent. Profile over the original phase Φ of Pair 2, the atmospheric component Φ_A with its associated confidence band ($\Phi_A \pm$ standard deviation, Std), and the corrected phase.

Validation of the Data Fusion

The four subsidence maps and their associated quality maps underwent the data fusion procedure. In a first step, the deformation values, which refer to different time intervals, were converted into velocities. The maps of the residuals obtained through the first LS adjustment were used to check the quality of the input deformation maps. The outlier rejection mainly concerned isolated pixels, probably affected by errors due to decorrelation noise. The relatively low data redundancy of the adjustment prevented a more advanced error analysis. It must in fact be underlined that due to coherence loss, the four maps do not fully overlap: there are portions of the considered area that are only covered by two deformation maps, where the error analysis is limited.

The compensated velocity field, obtained in the final LS adjustment, is shown in Figure 8. The black cross in the center of the image corresponds to the maximum deformation in the urbanized area, which was considered in the previous section for the validation of the single maps. This location corresponds to a relative subsidence maximum of about 1.9 cm/yr: the maximum, which equals 2.1 cm/yr, is located in an industrial area (left side in Figure 8). The stable area used for the atmospheric effect correction is indicated by a squared area in the bottom part of Figure 8. The geodetic data used for the validation only cover the urbanized area, which represents the most critical part of the subsidence. The DInSAR compensated velocity field was compared with the reference one, obtaining

Mean error (bias) = 0.16 cm/yr,

Standard deviation = 0.27 cm/yr.

The small magnitude of the bias again confirms the good quality of the atmospheric effect reduction. The relatively high standard deviation is mainly due to localized discrepancies between the DInSAR and reference velocity values that are a consequence of the above mentioned low data redundancy of the adjustment.

Conclusions

The quantitative monitoring of subsidences, which may provide a valuable support to decision makers, needs to be

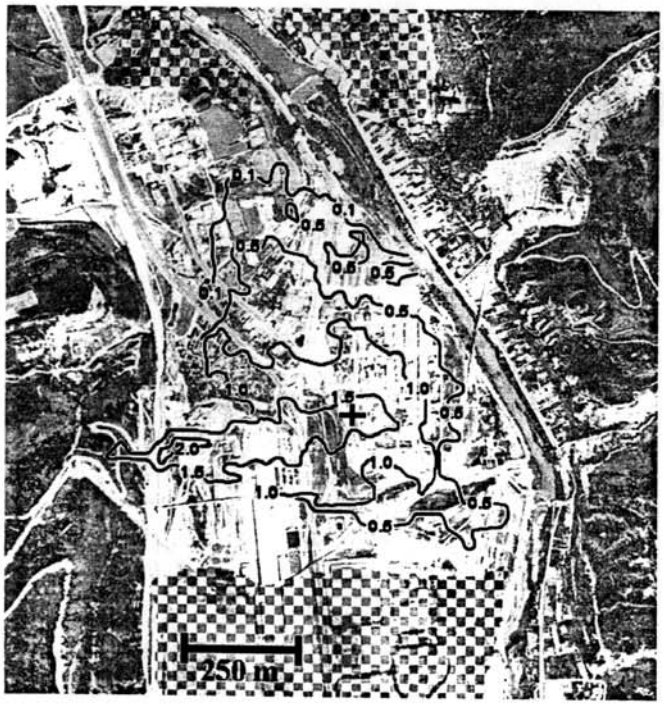

Figure 8. Sallent test case. Subsidence velocity field in [cm/yr], computed by LS adjustment from four DInSAR deformation maps, superimposed on a 1:25,000-scale orthoimage. The squared pattern indicates the stable areas located around the subsidence area. In the bottom part of the figure is located the stable area used for the atmospheric effect correction.

characterized by high quality standards. In this paper, the monitoring based on the DInSAR technique has been addressed. A complete DInSAR procedure has been described. Emphasis has been given to the description of the most original procedure components, which play a key role for the quantitative use of DInSAR: the LS calibration based on GCPs, which guarantees a high accuracy of the InSAR geometric model; the reduction of the atmospheric effects in small-scale subsidences; and the data fusion procedure for multiple observations of the same subsidence, which represents a key step to improve the quality of the DInSAR products.

The procedure has been validated over an urban subsidence area located in north eastern Spain. The considered case study was particularly suited to the validation for three reasons:

- it concerns an urban subsidence application related to risk assessment and public safety, which requires accurate and reliable measurements;
- the characteristics of the subsidence, like its slow deformation rate and its small spatial extent, make the DInSAR usage difficult; and
- precise and independent observations of the subsidence are available, which are suitable for performing a quantitative validation of the DInSAR results.

In the validation, the following aspects have been highlighted:

- the good geometric quality achieved through the InSAR calibration;
- the DInSAR capability to quantitatively discriminate, in urban areas, between subsidence and stable areas;
- the effectiveness of the procedure to reduce the atmospheric effects in DInSAR observations of small-scale subsidences; and
- the effectiveness of the data fusion procedure, which automatically takes into account the quality of the merged deformation maps.

The first results obtained with the ICC DInSAR procedure are encouraging. However, the goal of a fully quantitative subsidence monitoring requires further studies. A sensible improvement of the quality of the results should be achieved using a higher data redundancy (say, 10 or 15 pairs, instead of the four used in this work). Furthermore, it is necessary to focus on a strong limitation of the classical DInSAR technique: its use is limited to long-term coherent areas, such as urban areas. Beside these areas, the SAR images often contain isolated targets that remain coherent over very large time periods (Ferretti *et al.*, 2001). Using suitable unwrapping techniques, it is possible to exploit the interferometric phase over these targets (Costantini and Rosen, 1999). The integration of such techniques in the above-described DInSAR procedure should sensibly extend its applicability.

Acknowledgments

The authors thank Prof. Christian Tscherning of the University of Copenhagen, for kindly providing the GRAVSOFT package used for the collocation filtering and prediction of the atmospheric component.

References

Amelung, F., D.L. Galloway, J.W. Bell, H.A. Zebker, and R.J. Laczniak, 1999. Sensing the ups and downs of Las Vegas: InSAR reveals structural control of land subsidence and aquifer-system deformation, *Geology*, 27(6):483–486.

Amelung, F., S. Jonson, H.A. Zebker, and P. Segall, 2000. Widespread uplift and 'trapdoor' faulting on Galápagos volcanoes observed with radar interferometry, *Nature*, 407:993–996.

Baarda, W., 1968. A testing procedure for use in geodetic networks, *Publications on Geodesy, Vol. 5.*, Netherlands Geodetic Commission 2(5), Delft, Holland, 97 p.

Bamler, R., and P. Hartl, 1998. Synthetic aperture radar interferometry, *Inverse Problems*, 14:R1–R54.

Carnec, C., D. Massonnet, and C. King, 1996. Two examples of the use of SAR interferometry on displacement fields of small spatial extent, *Geophysical Research Letters*, 23(24):3579–3582.

Costantini, M., and P. Rosen, 1999. A generalized phase unwrapping approach for sparse data, *Proc. Int. Geosci. Remote Sensing Symp.*, Hamburg, Germany, 28 June–2 July, pp. 267–269.

Crosetto, M., 2002. Calibration and validation of SAR interferometry for DEM generation, *ISPRS Journal of Photogrammetry and Remote Sensing*, 57(3):213–227.

Crosetto, M., C.C. Tscherning, B. Crippa, and M. Castillo, 2002. Subsidence monitoring using SAR interferometry: Reduction of the atmospheric effects using stochastic filtering, *Geophysical Research Letters*, 29:26–29.

Dermanis, A., 1984. Kriging and collocation: A comparison, *Manuscripta Geodaetica*, 9(3):159–167.

El-Fiky, G.S., T. Kato, and Y. Fujii, 1997. Distribution of vertical crustal movement rates in the Tohoku district, Japan, predicted by least-squares collocation, *Journal of Geodesy*, 71: 432–442.

Ferretti, A., C. Prati, and F. Rocca, 2001. Permanent scatterers in SAR interferometry, *IEEE Transactions on Geoscience and Remote Sensing*, 39(1):8–20.

Ghiglia, D.C., and M.D. Pritt, 1998. *Two-Dimensional Phase Unwrapping: Theory, Algorithms and Software*, John Wiley and Sons, New York, N.Y., 493 p.

Goldstein, R.M., H. Englehardt, B. Kamb, and R.M. Frolich, 1993. Satellite radar interferometry for monitoring ice sheet motion: application to an Antarctic ice stream, *Science*, 262:1525–1530.

Goldstein, R.M., and C.L. Werner, 1998. Radar interferogram filtering for geophysical applications, *Geophysical Research Letters*, 25(21):4035–4038.

Hanssen, R., 2001. *Radar Interferometry*, Kluwer Academic Publishers, Dordrecht, Holland, 308 p.

Hellwich, O., and H. Ebner, 2000. Geocoding SAR interferograms by least squares adjustment, *ISPRS Journal of Photogrammetry and Remote Sensing*, 55:277–288.

Kimura, H., and Y. Yamaguchi, 2000. Detection of landslide areas using satellite radar interferometry, *Photogrammetric Engineering & Remote Sensing*, 66(3):337–344.

Kwok, R., and M.A. Fahnestock, 1996. Ice sheet motion and topography from radar interferometry, *IEEE Transactions on Geoscience and Remote Sensing*, 34(1):189–200.

Massonnet, D., M. Rossi, C. Carmona, F. Adragna, G. Peltzer, K. Felgl, and T. Rabaute, 1993. The displacement field of the Landers earthquake mapped by radar interferometry, *Nature*, 364: 138–142.

Massonnet, D., K. Feigl, M. Rossi, and F. Adragna, 1994. Radar interferometry mapping of deformation in the year after the Landers earthquake, *Nature*, 369:227–230.

Massonnet, D., P. Briole, and A. Arnaud, 1995. Deflation of Mount Etna monitored by spaceborne radar interferometry, *Nature*, 375:567–570.

Moritz, H., 1978. Least-squares collocation, *Reviews of Geophysics and Space Physics*, 16(3):421–430.

Patias, P. (editor) 1998. *ORFEAS: Optical-Radar Data Fusion for Environmental Applications*. Technical Report, Project ENV4-CT95-0150, EU Environmental and Climate Program, Department of Cadastre, Photogrammetry and Cartography, Aristotle University of Thessaloniki, Thessaloniki, Greece.

Peltzer, G., and P. Rosen, 1995. Surface displacement of the 17 May 1993 Eureka Valley, California, earthquake observed by SAR interferometry, *Science*, 268:1333–1336.

Strozzi, T., U. Wegmuller, L. Tosi, G. Bitelli, and V. Spreckels, 2001. Land subsidence monitoring with differential SAR interferometry, *Photogrammetric Engineering & Remote Sensing*, 67(11):1261–1270.

Tannous, I., and B. Pikeroen, 1994. Parametric modeling of spaceborne SAR image geometry. Application: SEASAT/SPOT image registration, *Photogrammetric Engineering & Remote Sensing*, 60(6):755–766.

Tesauro, M., P. Berardino, R. Lanari, E. Sansosti, G. Fornaro, and G. Franceschetti. 2000. Urban subsidence inside the city of Napoli (Italy) observed by satellite radar interferometry, *Geophysical Research Letters*, 27(13):1961–1964.

Tscherning, C.C., P. Knudsen, and R. Forsberg, 1994. *Description of the GRAVSOFT Package*, Technical Report, Geophysical Institute, University of Copenhagen, Copenhagen, Denmark.

(Received 10 October 2001; revised and accepted 30 September 2002)